Available online at www.sciencedirect.com
SCIENCE DIRECT
Journal of Molecular Catalysis A: Chemical 242 (2005) 48–56
JOURNAL OF MOLECULAR CATALYSIS A: CHEMICAL
www.elsevier.com/locate/molcata

Photodegradation of Congo Red catalyzed by nanosized TiO_2

Rajeev K. Wahi, William W. Yu*, Yunping Liu, Michelle L. Mejia, Joshua C. Falkner, Whitney Nolte, Vicki L. Colvin

Department of Chemistry, Rice University, 6100 Main Street, Houston, TX 77005, USA

Received 6 June 2005; accepted 27 July 2005
Available online 6 September 2005

Abstract

The effects of various physical properties (particle size, shape, surface area, crystal structure, and phase composition) on the photocatalytic performance of nanosized TiO_2 were studied through the photodegradation of Congo Red. Kinetic results showed that anatase TiO_2 was a superior photocatalyst to rutile TiO_2 due to the inherent difference in the two crystal structures. Anatase TiO_2 nanorods with predominantly (1 0 1) surface exhibited low activity because the non-dissociative adsorption of H_2O to this surface retarded the generation of $OH^{\bullet}$ radicals required for facile photocatalytic oxidation. It was found for the first time that the shape of TiO_2 nanocrystals significantly affected their photocatalytic activities. The previously reported anatase–rutile synergetic effect in commercialized mixed-phase TiO_2 (Degussa P25) was not observed in this study, perhaps, due to poor contact between the two phases and the extremely small sizes, as well as the not-optimized phase compositions in the current work.

Keywords: Photocatalysis; Congo Red; TiO_2; Nanoparticle; Catalysis

1. Introduction

Nanoscale materials possess distinctive properties differing from their molecular and bulk forms, such as quantum confinement [1,2], superparamagnetism [3], superior catalytic performances including the high selectivity and high reactivity [4–7]. The use of nanocrystalline TiO_2 in the photocatalytic oxidation of organic molecules represents a promising remediation strategy for wastewater systems. In the past decades, hundreds of reports have been published on TiO_2-mediated destruction of organic pollutants such as polychlorobiphenyls, toluene, surfactants, pesticides and their precursors, herbicides, phenols and phenolic compounds, carboxylic acids, halogenated hydrocarbons, aromatic sulfides, and organic dyes [8–17]. Given the enormous variety of organic compounds that can be photocatalytically degraded by TiO_2, there has naturally been a great interest in finding ways to improve the efficiency of TiO_2 in such processes.

In general, the efficiency or activity of a photocatalyst increases with its adsorptive capacity and the extent of charge separation upon photoinduced generation of electron–hole (e^-/h^+) pairs. Small particle size and high specific surface area tend to increase the photocatalytic activity of TiO_2 due to the large number of surface sites for adsorption and subsequent desorption of reactant molecules, although there might be limits to this beneficial effect since the recombination rate of e^-/h^+ may be high in extremely small particles [18–21]. Efficient charge separation is particularly critical since photogenerated holes are required for oxidation of adsorbents, usually through the mediation of an adsorbed OH^- group that reacts with a hole to form the powerful oxidant $OH^{\bullet}$ radical [22].

It is widely accepted that the anatase TiO_2 is a more efficient photocatalyst than the rutile TiO_2 because of the former's relatively high adsorptive affinity for organics and the superior hole-trapping ability [22–27]. However, it has also been shown that a commercialized mixture of the two phases (Degussa P25) exhibited much superior photocatalytic activity to pure-anatase and rutile TiO_2 [28–35]. This enhanced activity in mixed-phase catalysts results from a synergetic effect involving prolonged separation of photogenerated electrons and holes through interfacial electron transfer from the conduction band of rutile phase to the trapping states of anatase phase [33].

Despite the vast body of knowledge about the effects of TiO_2's physical properties on its photocatalytic behavior, a num-

* Corresponding author. Tel.: +1 713 348 3489; fax: +1 713 348 2578.
E-mail address: wyu@rice.edu (W.W. Yu).

1381-1169/$ – see front matter © 2005 Elsevier B.V. All rights reserved.
doi:10.1016/j.molcata.2005.07.034

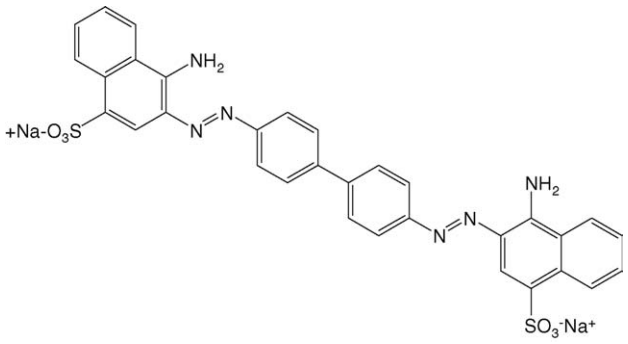

Scheme 1. Molecular structure of Congo Red.

ber of ambiguities questions remain. It is unclear that if the particle size (and therefore, the specific surface area) plays any effect when anatase is usually a better photocatalyst than rutile [33]. A second concern is whether the anatase–rutile synergy for Degussa P25 TiO_2 (particle size ~ 20 nm) would also be observed in other mixed-phase TiO_2 systems, especially those with ultrafine particle sizes (<10 nm). It is also not clear that if the relative amounts of anatase and rutile in TiO_2 catalysts would affect this synergetic effect. And, the influence of nanocrystal shape and dominant crystallographic surfaces on the photocatalytic activity of TiO_2 has not been thoroughly investigated. For example, it has been found that ZnO-mediated photocatalysis is more efficient on the (1 0 −1 0) surface than the (0 0 0 2) surface [36,37]. If TiO_2 were found to exhibit face-dependent activity, it would provide a valuable new way to optimize the photocatalytic performance of TiO_2 through the tuning of surface orientation. And thus, one could design a TiO_2 photocatalyst with dominant crystal faces that would be best for photocatalysis. Such a strategy would be especially useful to prepare oriented TiO_2 thin films photocatalyst.

A series of photocatalysis experiments with different particle size, specific surface area, and phase composition of nanosized TiO_2 were studied in this work in order to assess the effects of each factor on the photocatalytic activity of both single- and mixed-phase photocatalysts. Several techniques were modified to synthesize TiO_2 nanocrystals that allowed different physical properties to be tuned independently. This is in contrast to previous studies in which calcination was almost the only means to make TiO_2 nanocrystals, with the result that changes in particle size were accompanied by changes in such as phase composition and vice versa [38]. In addition, the effects of particle morphology on photocatalytic performance were studied for the first time by comparing the activities of isotropic and anisotropic anatase nanocrystals with different proportions of (1 0 1) surface sites.

2. Experimental

Photodecomposition of aqueous Congo Red (Scheme 1) was used as a model reaction to characterize photocatalytic behavior of different nanosized TiO_2. Congo Red is a recalcitrant azo dye found in textile wastewater. It has been the subject of several photocatalysis studies including TiO_2 [17,39–42]. Photocatalytic degradation of Congo Red proceeds in a way that nitrogen atoms from the azo functionality are liberated as molecular nitrogen rather than harmful nitrates. Thus, photocatalysis is a promising way to eliminate Congo Red and similar organic pollutants from the environment.

2.1. Chemicals

An anatase–rutile mixture TiO_2 powder (P25) was kindly supplied by Degussa Corporation. Ultrapure water (18.2 MΩ cm) was obtained from a Millipore purification system. Tetramethylammonium hydroxide (TMAH), titanium(IV) isopropoxide (99.999%), titanium(IV) chloride (99.995%), Congo Red (85%), and 2-propanol (99.5%) were purchased from Aldrich; titanium(IV) ethoxide (97%) was from Fluka; dry ethanol was from Pharmco; hydrochloric acid, sodium hydroxide, and sodium chloride were from Fisher. All chemicals were used as-received.

2.2. Preparation of nanosized TiO_2 photocatalyst powders

The reaction conditions used to prepare nine different nanosized TiO_2 powders used in this study were summarized in Table 1. Symbol A for TiO_2 powder (catalyst) means anatase phase, R means rutile phase, AR means the mixture of anatase and rutile phases, and Rod means rod-like shapes (though they are anatase).

2.2.1. Anatase spherical dots of nanosized TiO_2 powders

Anatase spherical dots of nanosized TiO_2 with different particle sizes (A1, A2, and A3) were prepared by hydrothermal method. A known amount of ultrapure water was mixed with ethanol and heated in a 450 mL Monel autoclave (Parr Instruments). Once the mixture in the autoclave reached the desired temperature (see Table 1), a dry ethanol solution of titanium(IV) ethoxide was transferred into the autoclave. The total reaction volume was 100 mL and the molar ratio of water to titanium(IV) ethoxide was 20:1. The reaction mixture was stirred at a constant temperature for 2 h and then quenched by putting the autoclave into a coldwater bath. The product was filtered, washed twice with pure water, and dried overnight at 60 °C.

2.2.2. Ultrafine rutile and mixed-phase nanosized TiO_2 powders

One TiO_2 powder of pure rutile (R1) and two anatase–rutile mixtures (AR1 and AR2) were prepared using a modified method reported by Cheng et al. [43] Typically, titanium(IV) chloride (47.0 g, 0.25 mol) was added slowly to ultrapure water (450 mL) to produce a white suspension. Hydrochloric acid (37.5%, 50 mL) was added to the suspension as a peptizing agent, and stirred overnight to get a clear solution. The peptized TiO_2 suspension was adjusted to the desired pH (pH 1 for R1, pH 0.25 for AR1 and AR2) by addition of aqueous sodium hydroxide; then it was heated and refluxed for 2 h. The TiO_2 particles were precipitated out of the suspension by adding solid sodium chloride. The TiO_2 powder was collected by centrifugation, washed twice with ultrapure water, and dialyzed in several successive ultrapure water baths for a total time of 24 h. The final powder was dried overnight at 60 °C.

Table 1
Synthesis of nanosized TiO2 photocatalysts

Catalyst	Precursor (concentration, mol L^{-1})	Solvent	Temperature (°C)	Reaction time (h)	Particle shape	Phase[a]	Average diameter (nm)	Surface area ($m^2\ g^{-1}$)
P25	N/A	N/A	N/A	N/A	Spherical dot	A/R (80/20)	21	50
A1	$Ti(OEt)_4$ (0.02)	EtOH	140	2	Spherical dot	A	5.5	251
A2	$Ti(OEt)_4$ (0.32)	EtOH	150	2	Spherical dot	A	10.1	153
A3	$Ti(OEt)_4$ (0.02)	EtOH	220	2	Spherical dot	A	15.1	83.5
R1	$TiCl_4$ (0.5)	H_2O	100	2	Spherical dot	R	5.4	110
AR1	$TiCl_4$ (0.5)	H_2O	100	2	Spherical dot	A/R (40/60)	5.2 (A) 5.4 (R)	232
AR2	$TiCl_4$ (0.5)	H_2O	100	2	Spherical dot	A/R (70/30)	5.2 (A) 5.0 (R)	123
Rod1[b]	$Ti(^iOPr)_4$ (0.76[c])	H_2O	90–100[d] 180–190[f]	6[d] 5[f]	Short rod	A	50[e]	94.5
Rod2[g]	$Ti(^iOPr)_4$ (0.76[c])	H_2O	90–100[d] 180–190[f]	6[d] 5[f]	Long rod	A	200[e]	28.0

[a] A: anatase; R: rutile. Mass ratios of A/R were listed in the parathesis.
[b] Synthesized with 0.17 mmol L^{-1} tetramethylammonium hydroxide (TMAH).
[c] In the unit of mmol L^{-1}.
[d] First reaction temperature with 6 h.
[e] Long axis.
[f] Following reaction temperature with 5 h.
[g] Synthesized with 0.91 mmol L^{-1} TMAH.

2.2.3. Anatase TiO_2 nanorods with different lengths

Anatase TiO_2 nanorods were synthesized with a surfactant [44]. Briefly, a water solution of TMAH (1500 mL) was prepared in a 2000 mL, three-neck flask and was cooled to 4–5 °C in an water–ice bath; then a solution of titanium(IV) isopropoxide (3.33 mL, 1.14 mmol) in 2-propanol (100 mL) was poured into the flask. The resulting turbid white suspension was stirred at ~8 °C for 10 min first, and then heated at 90–100 °C for 6 h. Coarsening of the TiO_2 nanoparticles to obtain rod-like nanocrystallites was accomplished by heating the suspension for another 5 h at 180–190 °C. The resulting nanorods were crashed out of the suspension, centrifuged, washed, dialyzed, and dried as described above. TMAH was completely removed from the nanorod samples, which was confirmed by Fourier Transform Infrared (FT-IR) spectroscopy (see Fig. 5 and the related discussion).

2.3. Characterization of nanosized TiO_2 powders

All TiO_2 powders were characterized using X-ray diffraction (XRD), transmission electron microscopy (TEM), Brunauer–Emmett–Teller (BET) surface area analysis, and differential thermal analysis (DTA).

XRD patterns were taken through a Siemens platform-model general area detector diffraction system (GADDS) with a Cu Kα source. The powder samples were run with silicon powder (as an internal standard) to account for instrumental line broadening when calculating particle sizes from the TiO_2 linewidths. Particle sizes were calculated according to the Debye–Scherrer formula with Warren's correction for instrumental broadening [45]:

$$D\,(\text{Å}) = \frac{0.89\lambda}{\beta\,\cos\theta_B} \quad (1)$$

where D is the crystallite size, λ is the X-ray wavelength (1.54 Å for Cu Kα radiation), and θ_B is the Bragg angle. The parameter β is defined as $\beta \equiv (B^2 - b^2)^{1/2}$, where B and b are the linewidths of the most intense TiO_2 reflection ((1 0 1) for anatase, (1 1 0) for rutile) and the (1 1 1) line of the silicon standard, respectively. Calculation of average particle sizes from XRD linewidths was adapted in the case of the anatase dots, the rutile dots, and the laboratory-synthesized anatase–rutile mixtures. Crystallite sizes in the other samples with larger than 20 nm was done using TEM instead.

BET surface areas were measured from N_2 adsorption using a Micromeritics ASAP 2010 apparatus. Samples were degassed for 5 h prior to the N_2 adsorption analysis.

TEM pictures were taken on a JEOL 2010 microscope. TEM sample was prepared by dropping one to two drops of sonicated suspension of TiO_2 onto a 300-mesh carbon-coated copper grid and then evaporated the solvent. The average particle sizes were obtained by measuring 500–1000 individual particles from the TEM images using Image-Pro Plus 5.0 (Media Cybernetics Inc.) [3,46].

DTA was performed in air on a Thermal Advantage SDT 2960 apparatus from 25 to 600 °C at a heating rate of 20 °C min^{-1}.

2.4. Photocatalytic degradation of Congo Red with nanosized TiO_2

The adsorption isotherms for Congo Red onto TiO_2 powders showed that it took considerably long time (>20 h) for Congo Red to reach adsorption equilibrium onto all the nine self-made TiO_2 catalysts, while less than 1 h onto P25 (Fig. 1). So, the water suspensions of Congo Red and nanosized TiO_2 powders was stirred in the dark for 24 h (1 h for Degussa P25) to ensure the adsorption equilibrium was established prior to irradiation. Photocatalytic reactions were then carried out inside a Luzchem model 4-V photoreactor equipped with a magnetic stirrer and

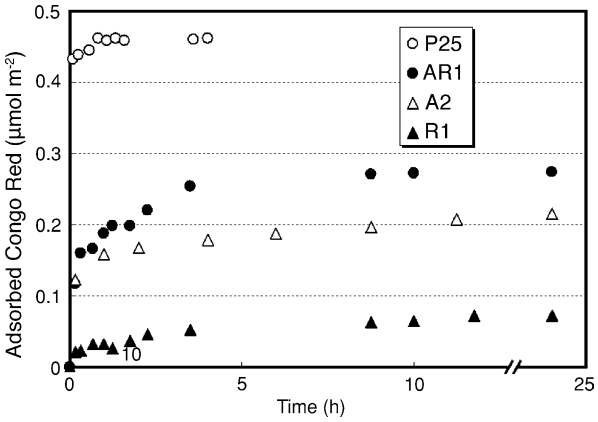

Fig. 1. Adsorption isotherms of Congo Red (72 μmol L^{-1}) on nanosized TiO_2 photocatalysts.

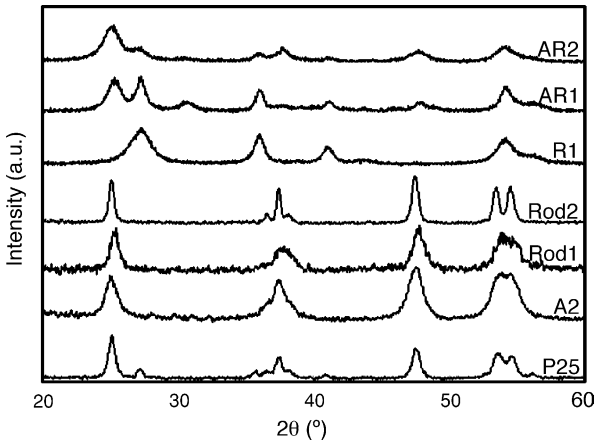

Fig. 2. X-ray diffraction patterns of nanosized TiO_2 photocatalysts.

14 UV-A lamps with an emission maximum at λ = 350 nm. In all cases, the TiO_2 concentration was 1.0 g L^{-1} and the total water suspension volume was 10.0 mL. Initial Congo Red concentrations varied from 1.0 to 30 mg L^{-1}. The disappearance of Congo Red was monitored using the UV–vis absorbance feature at λ = 496 nm as a function of irradiation time. Congo Red concentrations were then calculated from the absorbances of the Congo Red–TiO_2 suspensions (the contribution of TiO_2 to the UV–vis spectra of Congo Red was subtracted).

The photocatalytic efficiency (activity) of each TiO_2 catalyst for the degradation of Congo Red was quantified in two ways: measurement of Congo Red half-life time under standard conditions and Langmuir–Hinshelwood kinetic analysis. In this study, the Congo Red half-life time, $t_{1/2}$, was defined as the amount of time required for photocatalytic degradation of 50% of the Congo Red in a 10 mg L^{-1} (14 μmol L^{-1}) aqueous Congo Red solution when a TiO_2 catalyst was present at a concentration of 1 g L^{-1}. Surface catalyzed reactions can often be adequately described by a unimolecular Langmuir–Hinshelwood mechanism, in which an adsorbed reactant with fractional surface coverage θ is consumed at an initial rate given by:

$$-\left.\frac{dC}{dt}\right|_0 = r_0 = k\theta = \frac{kKC_0}{1+KC_0} \quad (2)$$

where k is a rate constant that changes with photocatalytic activity, K the adsorption equilibrium constant, and C_0 is the initial concentration of the reactant (Congo Red in this case). Inversion of the above rate equation gives:

$$\frac{1}{r_0} = \frac{1}{kK}\frac{1}{C_0} + \frac{1}{k} \quad (3)$$

Thus, a plot of r_0^{-1} against C_0^{-1} should be a straight line with a slope of $(kK)^{-1}$ and an intercept of k^{-1} [23]. Such analysis allows one to quantify the photocatalytic activity of a TiO_2 catalyst through the rate constant k, with larger k values corresponding to higher photocatalytic activity. Adsorption equilibrium constant K accounts for the adsorptive ability of a TiO_2 catalyst.

It is important to note that the above unimolecular analysis does not take into account the concentration of the $OH^\bullet$ radicals involved in the photocatalytic oxidation. However, one can treat [$OH^\bullet$] as essentially a constant if [$OH^\bullet$] is much larger than C_0, and therefore [$OH^\bullet$], can be left out of the rate expression [47]. As will be seen below, the unimolecular Langmuir–Hinshelwood analysis was good at lower initial Congo Red concentrations (C_0) but failed at higher C_0 values in the present study. Although a bimolecular Langmuir–Hinshelwood analysis would be more appropriate than the unimolecular analysis at high C_0, there is no good way to quantify the $OH^\bullet$ concentration on the TiO_2 surfaces.

3. Results and discussion

3.1. Characterization of nanosized TiO_2 photocatalyst powders

Characteristic properties of all the nanosized TiO2 photocatalysts were summarized in Table 1. XRD patterns of TiO_2 powders (Fig. 2) indicate that Rod1, Rod2, and A1, A2, and A3 were pure-anatase structure (A1 and A3 not shown), while R1 was pure rutile structure. Degussa P25, AR1, and AR2 were mixed-phase powders with anatase/rutile mass ratios of approximately 80/20, 40/60, and 70/30, respectively. Small amounts of brookite (<5%) were also detected in the AR1 and AR2 samples. None of the DTA profiles exhibited an exothermic peak between 350 and 450 °C, thus, confirmed the 100% crystallinity of all the powders (Fig. 3).

It can be seen from TEM images (Fig. 4) that the particles prepared in the presence of TMAH surfactant (Rod1 and Rod2) were significantly less aggregated than those prepared without surfactant. The use of HCl as a peptizing agent during the synthesis of the rutile and mixed-phase powders could not prevent from the aggregation in these materials (R1, AR1, and AR2). In fact, aggregation among the rutile nanocrystals was so prevalent that many of the particles in R1 formed large, loose, striated structures. And, in contrast to the spherical morphologies of TiO_2 prepared without TMAH (A2, R1, AR1, and AR2), the Rod1 and Rod2 nanocrystals exhibited striking rod-like morphologies, and larger aspect ratios and larger particles produced with high surfactant concentrations (Rod2) than low surfactant concentrations (Rod1).

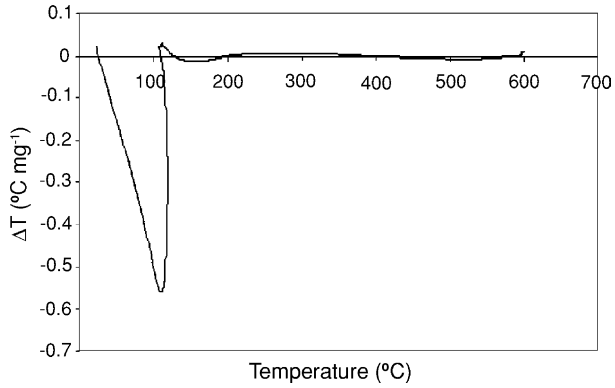

Fig. 3. DTA profile of A2 nanosized TiO_2 photocatalyst. The endothermic peak near 100 °C corresponds to the evaporation of adsorbed water, while the absence of a sharp exothermic peak between 350 and 450 °C indicates the 100% crystallinity (i.e., no amorphous phase) of the nanosized TiO_2 powder.

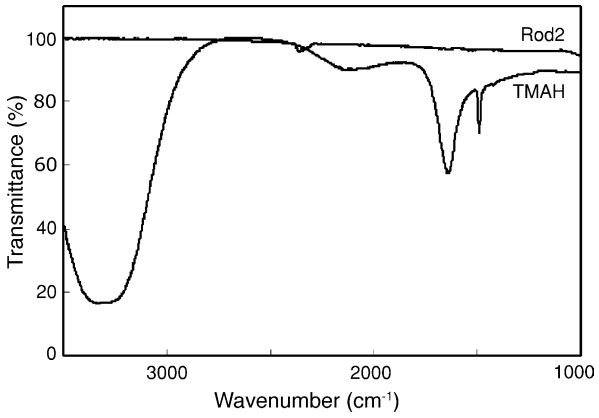

Fig. 5. FTIR spectra of TMAH and Rod2. The absence of characteristic TMAH resonances in Rod2 confirms that TMAH was completely removed from nanorod surfaces.

BET surface areas ranged from 28 to 251 m^2g^{-1} in the 10 nanosized TiO_2 powders studied here. Generally, powder with smaller particle size had higher surface area. But R1 and AR2 had only about 50% surface area (110–123 m^2g^{-1}) of A1 (251 m^2g^{-1}) with similar particle size ($\sim$ 5 nm), largely due to the extensive aggregation of those particles (Fig. 4).

The absence of any characteristic TMAH peaks in the FTIR spectrum of anisotropic Rod1 indicated that the TMAH surfactant was completely removed from the nanocrystal surfaces by washing and dialyzing (Fig. 5). The same spectrum as Rod1 was also observed for Rod2 (not shown).

3.2. Photocatalytic decomposition of Congo Red over nanosized TiO_2 photocatalysts

The photocatalytic activity of each TiO_2 catalyst was quantified using the half-life time ($t_{1/2}$) for a 10 mg L^{-1} (14 μmol L^{-1}) Congo Red solution and the Langmuir–Hinshelwood rate constant (k). The values of $t_{1/2}$ and k were expressed on both a unit mass basis ($t_{1/2,m}$, k_m) and a unit surface area basis ($t_{1/2,s}$, k_s). Activities evaluated on a unit mass basis reflected largely the influence of surface area on a catalyst's performance, while activities expressed on a unit surface area basis (i.e., specific activities) reflected the effects of physical properties other than surface area.

The Congo Red decomposition curves indicate that the A2, A3 and P25 catalysts had similar activity ($t_{1/2,m}$ = 1.5–3.5 min g) on a mass basis, while the mixed-phase powders AR1 and AR2 had a little longer half-life time ($t_{1/2,m} \cong$ 5 min g) (Fig. 6 and Table 2). In contrast, the photocatalytic reaction was considerably slower ($t_{1/2,m}$ = 15–30 min g) over Rod1 and Rod2 anatase nanorods. And, very slow photodegradations of Congo Red were observed over rutile R1 ($t_{1/2,m}$ = 120 min g). The mass-based activities ($t_{1/2,m}$) of the TiO_2 catalysts increased in the order R1 < A1 < Rod2 < Rod1 < AR1 ≅ AR2 < P25 < A3 (A2. The surface area-based activities ($t_{1/2,s}$) of TiO_2 catalysts were also calculated and had basically the same trend as the mass-based activities (Table 2).

The initial rate (r_0) of Langmuir–Hinshelwood analysis provides an additional quantitative comparison of the photocatalytic activity of TiO_2. An important issue to address first, however, is the initial Congo Red concentration (C_0) limits

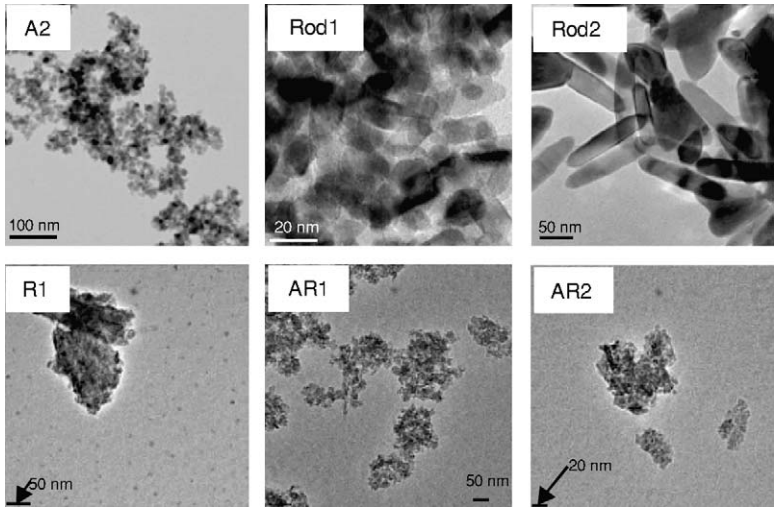

Fig. 4. TEM pictures of nanosized TiO_2 photocatalysts.

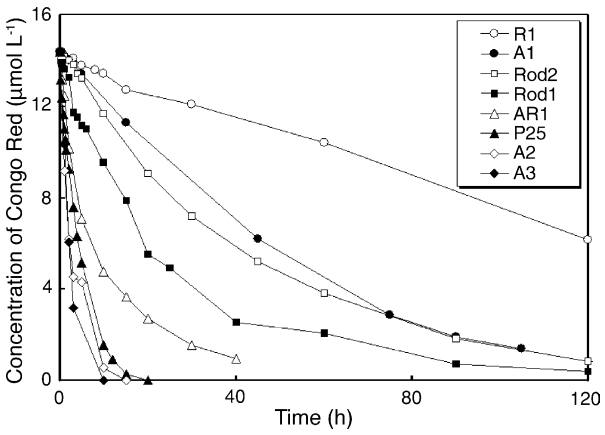

Fig. 6. Photodegradation of Congo Red catalysed by nanosized TiO_2.

to the applicability of the Langmuir–Hinshelwood model in different systems. This can be assessed by examining the linearity of a plot of r_0^{-1} versus C_0^{-1} for each catalyst. Fig. 7 shows curves of $r_0 - C_0$ (Fig. 7a) and $r_0^{-1} - C_0^{-1}$ (Fig. 7b) for two TiO_2 catalysts (AR1 and R1) over a wide range of initial Congo Red concentrations tested. The concentration ranges over which the reciprocal plots (Fig. 7c) were linear in accordance with Langmuir–Hinshelwood model were specified in Table 2. Langmuir–Hinshelwood model were good over wide ranges for highly active photocatalysts, e.g., A2, A3, and P25, presumably, because the generation rates of $OH^{\bullet}$ in those TiO_2 catalysts were fast enough to meet the unimolecular Langmuir–Hinshelwood model's assumption of a large, essentially constant concentration of $OH^{\bullet}$ relative to the Congo Red concentration. On the other hand, low-activity catalysts such as R1 generated $OH^{\bullet}$ very slowly; the unimolecular Langmuir–Hinshelwood model's requirement was only met when C_0 was low.

The rate constant k and the adsorption equilibrium constant K were obtained through linear fits (Fig. 7c). For most TiO_2 catalysts, the order of photocatalytic activity quantified by rate constant k was generally in agreement with the order of activity quantified by $t_{1/2}$ (Table 2). In cases where the k value contradicted the $t_{1/2}$ result, $t_{1/2}$ was assumed to be more reliable measurement of photocatalytic activity and used in the follow-

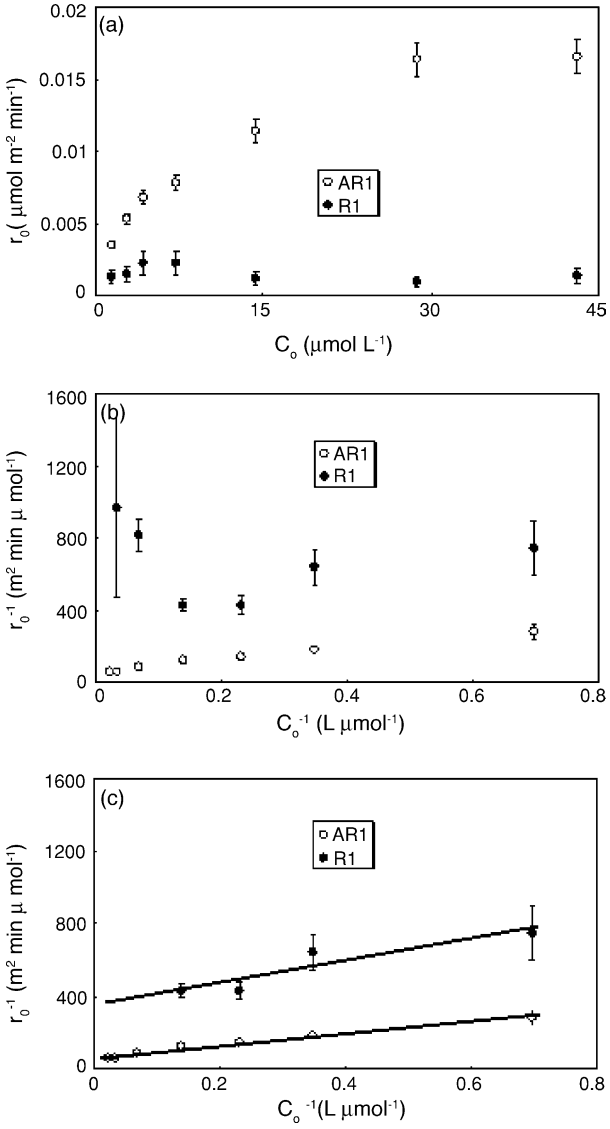

Fig. 7. Langmuir–Hinshelwood analysis of Congo Red photodegradation: (a) r_0 vs. C_0 on a unit surface area basis; (b) reciprocal plots on a unit surface area basis; (c) fitting the linear portions of the reciprocal plots to determine the parameters k and K.

Table 2
Kinetic parameters in Congo Red photodegradation over nanosized TiO_2 photocatalysts

Sample	$t_{1/2,m}$[a] (min g)	$t_{1/2,s}$[b] (min m^2)/10^2	Maximum C_0[c] (μmol L^{-1})	k_m[d] (μmol g^{-1} min^{-1})	k_s[e] (μmol m^{-2} min^{-1})/10^{-2}	K (μmol g^{-1})
P25	3.5	1.75	30	4.08	8.15	0.235
A1	40	100	–	–	–	–
A2	1.5	2.30	≥40	5.11	3.34	0.206
A3	1.75	1.46	–	–	–	–
R1	120	–	∼5	1.60	1.46	0.027
AR1	5	11.6	≥40	3.57	1.54	0.199
AR2	5	6.15	–	–	2.5	–
Rod1	15	14.2	15	1.80	1.90	0.068
Rod2	30	8.40	20	0.47	1.67	0.230

[a] Half-life time expressed on a unit mass basis.
[b] Half-life time expressed on a surface area basis.
[c] Maximum initial Congo Red concentration for unimolecular Langmuir–Hinshelwood analysis applicability.
[d] Rate constant expressed on a unit mass basis.
[e] Rate constant expressed on a surface area basis.

ing discussion, because the determination of $t_{1/2}$ required fewer calculations and approximations than the determination of k.

3.2.1. Effects of particle size and surface area

The kinetic data for the spherical dot-shaped anatase catalysts (A1, A2, and A3) indicated that particle size and surface area were the two most important factors influencing the photocatalytic activity of nanocrystalline TiO_2 catalyst (Table 2). The $t_{1/2,m}$ for the 15.1 nm (A3) and 10.1 nm (A2) nanodots were both about 1.5 min g, while $t_{1/2,m}$ for the 5.5 nm nanodots (A1) was 40 min g. Thus, 10–15 nm nanodots with low to intermediate surface areas (80–150 $m^2\ g^{-1}$) were about 25 times more active than 5.5 nm nanodots with very high surface area (251 $m^2\ g^{-1}$). This shows that despite the larger number of surface sites available for Congo Red adsorption onto smaller nanodots, the increased recombination rate of e^-/h^+ in very small particles resulted in an overall decrease in photocatalytic activity. The 10.1 nm nanodots of A2 ($t_{1/2,m}$ = 1.5 min g) were slightly more active than the 15.1 nm nanodots of A3 ($t_{1/2,m}$ = 1.75 min g), indicating that A2's larger surface area contributed more in photocatalytic activity than electron–hole separation when the particle was big enough (>10 nm). It appears to be an optimal particle size of about 10 nm for a maximum photocatalytic activity of anatase nanodots.

3.2.2. Effect of phase composition

3.2.2.1. Single-phase catalysts: anatase versus rutile. The single-phase anatase catalysts exhibited widely varied activities that appeared to depend not only on particle size and surface area but also on the surface (crystal) structure. It can be concluded from $t_{1/2,}$ data that anatase TiO_2 is a better photocatalyst than rutile TiO_2. The $t_{1/2,}$ values for the anatase TiO_2 were found to be about 2–100 times smaller than that of the 5.4 nm R1 rutile nanodots, indicating that the surface of anatase is better to photocatalysis than the surface of rutile. Thus, the generally superior photocatalytic activity of anatase is not merely a result of the typically easy-achieved larger surface areas, but rather a result of the fundamental differences between the anatase and rutile surfaces (crystal structures). Specifically, the poor activity of R1 suggests that even a moderately high surface area (110 $m^{-2}\ g^{-1}$) cannot compensate for the inefficient hole trapping and low adsorptive affinity that typically related with rutile's inherent crystal structure.

The adsorption isotherms in Fig. 1 showed the low adsorptive affinity of rutile TiO_2 for Congo Red, thus, lowered the activity of R1 in photocatalytic degradation of Congo Red. In addition, the low apparent adsorption constant K obtained from Langmuir–Hinshelwood analysis for R1 (K = 0.027) confirms its low adsorptive affinity.

3.2.2.2. Synergetic effect of anatase–rutile mixed-phase TiO_2 catalysts. Our experiments confirmed the strong synergetic effect in enhancing the photocatalytic activity of P25. In the terms of $t_{1/2}$ and k, it was found that P25, an anatase–rutile mixture with an intermediate surface area (50 $m^2\ g^{-1}$), was more active than A2, a pure-anatase powder with higher surface area (153 $m^2\ g^{-1}$), by a factor of 2.5. Thus, it is clear that the presence of two phases in P25 resulted in a remarkable increase in photocatalytic activity over pure-anatase TiO_2.

However, this synergetic effect was not apparent in the ultrafine anatase–rutile mixture AR1 and AR2 (∼5 nm) despite their high surface areas (123–232 $m^2\ g^{-1}$). They were even less active than pure-anatase A2 and A3. The $t_{1/2}$ and Langmuir–Hinshelwood rate constant k supported this observation.

There are several possible reasons for the absence of synergetic effect in our anatase–rutile mixtures. First, the photocatalytic activity of such mixtures depends in part on the relative amounts of these two phases. Bacsa and Kiwi reported that a highest activity for *p*-coumaric acid degradation was observed for an anatase/rutile ratio of 70/30 [29]. It is possible that AR1 exhibited low photocatalytic activity because of not-optimized anatase/rutile ratio (40/60). However, AR2 performed almost the same activity as AR1 even its anatase/rutile ratio (70/30) was close to that of P25 (80/20) and equal to the optimal composition reported by Bacsa and Kiwi.

A more important factor is likely the anatase–rutile interface in these two catalysts. The enhancement of activity in Degussa P25 has been attributed to efficient electron transfer from rutile to anatase, which increases the charge separation needed for efficient photocatalytic reaction at the particle surfaces [33]. Well-contacted interfaces between the anatase and rutile phases would thus be essential for an appreciable increase in photocatalytic activity for any mixed-phase catalysts [32,48]. But the anatase–rutile interfacial contacts in AR1 and AR2 may not be well controlled as P25. And the smaller size (5 nm) in AR1 and AR2 may not be good for the electron-hole separation for a high activity (see Section 3 for A1).

3.2.3. Effect of morphology on the activity of anatase TiO_2 catalysts

TiO_2 nanorods (Rod1 and Rod2) performed significantly worse than the anatase nanodots (A2 and A3) (Table 2). Specific activities, as quantified by $t_{1/2,}$ and k, indicated that nanorods were 5–10 times less active than the 10–15 nm nanodots. FTIR spectroscopy confirmed the complete removal of surfactant from the nanorods samples prior to the photocatalytic experiments (Fig. 5), so surfactant poisoning or retarding could be ruled out as a reason for the poor performance of the Rod1 and Rod2 catalysts. The surface areas accounted partially for the differences in their per mass activities, but cannot account for all the activity difference. A (1 0 1) surface dominated TiO_2 was obtained by selective binding of the tetramethylammonium cation ($N(CH_3)_4^+$) to the (1 0 1) surface, which inhibited the growth in the [1 0 1] direction and promoted the growth in perpendicular directions [44]. The higher the surfactant concentration, the more pronounced this anisotropic effect. So, the dominated (1 0 1) surface sites in Rod1 and Rod2 seemed unfavorable to the photocatalytic activity of TiO_2.

The deleterious effect of (1 0 1) surfaces on photocatalytic activity could be derived from the water adsorption modes to different anatase surfaces. Theoretical calculations have indicated that water molecules tend to adsorb dissociatively (i.e., as H^+ and OH^-) to anatase (0 0 1) but non-dissociatively (i.e., as

H_2O) to anatase (1 0 1) facet [49,50]. Thus, in turn, the number of $OH^{\bullet}$ radicals generated from OH^- upon irradiation would be less on (1 0 1) facet. Because $OH^{\bullet}$ radicals are thought to be the primary oxidizing species in photocatalytic oxidation reactions, it follows that anatase (1 0 1) surface is less active in such reactions than (0 0 1) or other surfaces to which water adsorbs in a primarily dissociative fashion.

4. Summary

The photoinduced decomposition of Congo Red in aqueous solution over 9 different nanocrystalline TiO_2 photocatalysts were studied on a series of effects, including particle size, surface area, phase composition, and morphology. Photocatalytic activity was quantified using both half-life time measurements ($t_{1/2}$) and Langmuir–Hinshelwood kinetics (k).

Among the three anatase dots, the maximum photocatalytic activity was observed in A2 with intermediate particle size of ∼10 nm, suggesting a best balance between the charge separation and the surface area. Ultrafine rutile exhibited low activity despite its high surface area; this could be mainly attributed to the poor hole trapping ability generally observed in rutile catalysts. Thus, the superior photocatalytic activity of anatase TiO_2 is due to the inherent difference between the crystal structures of anatase and rutile, rather than the usually easy-obtained higher surface area of anatase TiO_2.

The anatase–rutile synergetic effect reported previously for Degussa P25 was again confirmed; however, this effect was not observed in our fine (∼5 nm) anatase–rutile mixtures, indicating that this synergetic effect requires optimal size and perhaps an optimal phase composition with good contact between the two phases.

It was also demonstrated for the first time that the photocatalytic activity of anatase greatly depends on particle morphology. Specifically, both the activities per mass and per surface area in the anatase nanocrystals with predominant (1 0 1) surface were lower than those in the isotropic anatase nanoparticles. This was because the non-dissociative adsorption of water to the (1 0 1) surface minimized the number of surface adsorbed hydroxyl groups that were then converted into hydroxyl radicals—an essential procedure in photocatalytic oxidation reactions.

Further study on nanocrystalline TiO_2 photocatalysts is undergoing in the lab, including the size and composition optimizing of the mixed-phase catalyst to get better synergetic effect.

Acknowledgement

This work was supported by the National Science Foundation through Center for Biological and Environmental Nanotechnology at Rice University (EEC-0118007).

References

[1] W.W. Yu, X. Peng, Angew. Chem. Int. Ed. 41 (2002) 2368.
[2] W.W. Yu, Y.A. Wang, X. Peng, Chem. Mater. 15 (2003) 4300–4308.
[3] W.W. Yu, J.C. Falkner, C.T. Yavuz, V.L. Colvin, Chem. Commun. (2004) 2306–2307.
[4] W. Yu, H. Liu, X. An, J. Mol. Catal. A Chem. 129 (1998) L9–L13.
[5] W. Yu, H. Liu, X. An, X. Ma, Z. Liu, L. Qiang, J. Mol. Catal. A Chem. 147 (1999) 73.
[6] W. Yu, H. Liu, Q. Tao, Chem. Commun. (1996) 1773–1774.
[7] W. Yu, M. Liu, H. Liu, X. An, Z. Liu, X. Ma, J. Mol. Catal. A Chem. 142 (1999) 201–211.
[8] E. De Felip, F. Ferri, C. Lupi, N.M. Trieff, F. Volpi, A. di Domenico, Chemosphere 33 (1996) 2263–2271.
[9] M.C. Blount, J.L. Falconer, Appl. Catal. B Environ. 39 (2002) 39–50.
[10] H. Hidaka, J. Zhao, E. Pelizzetti, N.J. Serpone, Phys. Chem. 96 (1992) 2226–2230.
[11] M.K.S. Mak, S.T. Hung, Toxicol. Environ. Chem. 36 (1992) 155–168.
[12] A. Sclafani, L. Palmisano, M. Schiavello, J. Phys. Chem. 94 (1990) 829–832.
[13] S.-J. Tsai, S. Cheng, Catal. Today 33 (1997) 227–237.
[14] H. Kominami, J. Kato, M. Kohno, Y. Kera, B. Ohtani, Chem. Lett. 1996 (1996) 1051–1052.
[15] C.S. Turchi, D.F. Ollis, J. Catal. 119 (1989) 483–496.
[16] T. Tachikawa, S. Tojo, M. Fujitsuka, T. Majima, J. Phys. Chem. B 108 (2004) 5859–5866.
[17] H. Lachheb, E. Puzenat, A. Houas, M. Ksibi, E. Elaloui, C. Guillard, J.M. Herrmann, Appl. Catal. B Environ. 39 (2002) 75–90.
[18] M.R. Hoffmann, S.T. Martin, W. Choi, D.W. Bahnemann, Chem. Rev. 95 (1995) 69–96.
[19] C.-C. Wang, Z. Zhang, J.Y. Ying, Nanostruct. Mater. 9 (1997) 583–586.
[20] L. Cao, A. Huang, F.-J. Spiess, S.L. Suib, J. Catal. 188 (1999) 48–57.
[21] C.B. Almquist, P. Biswas, J. Catal. 212 (2002) 145–156.
[22] A.L. Linsebigler, G.Q. Lu, J.T. Yates, J. Chem. Rev. 95 (1995) 735–758.
[23] M.A. Fox, M.T. Dulay, Chem. Rev. 93 (1993) 341–357.
[24] K.E. Karakitsou, X.E. Verykios, J. Phys. Chem. 97 (1993) 1184–1189.
[25] K. Tanaka, M.F.V. Capule, T. Hisanaga, Chem. Phys. Lett. 187 (1991) 73–76.
[26] B. Ohtani, S.J. Nishimoto, Phys. Chem. 97 (1993) 920–926.
[27] S.C. Jung, N. Imaishi, Kor. J. Chem. Eng. 18 (2001) 867–872.
[28] R.I. Bickley, T. Gonzalez-Carreno, J.T. Lees, L. Palmisano, R.J.D. Tilley, J. Solid State Chem. 92 (1991) 178–190.
[29] R.R. Bacsa, J. Kiwi, Appl. Catal. B Environ. 16 (1998) 19–29.
[30] T. Lopez, R. Gomez, E. Sanchez, F. Tzompantzi, L. Vera, J. Sol–Gel Sci. Technol. 22 (2001) 99–107.
[31] T. Kawahara, Y. Konishi, H. Tada, N. Tohge, J. Nishii, S. Ito, Angew. Chem. Int. Ed. 41 (2002) 2811–2813.
[32] T. Ohno, K. Tokieda, S. Higashida, M. Matsumura, Appl. Catal. A Gen. 244 (2003) 383–391.
[33] D.C. Hurum, A.G. Agrios, K.A. Gray, T. Rajh, M.C. Thurnauer, J. Phys. Chem. B 107 (2003) 4545–4549.
[34] B. Sun, P.G. Smirniotis, Catal. Today 88 (2003) 49–59.
[35] G. Balasubramanian, D.D. Dionysiou, M.T. Suidan, I. Baudin, J.-M. Laine, Appl. Catal. B Environ. 47 (2004) 73–84.
[36] D. Li, H. Haneda, Chemosphere 51 (2003) 129–137.
[37] Y. Yamaguchi, M. Yamazaki, S. Yoshihara, T.J. Shirakashi, Electroanal. Chem. 442 (1998) 1–3.
[38] Z. Ding, G.Q. Lu, P.F. Greenfield, J. Phys. Chem. B 104 (2000) 4815–4820.
[39] C. Hachem, F. Bocquillon, O. Zahraa, M. Bouchy, Dyes Pigments 49 (2001) 117–125.
[40] C. Guillard, J. Disdier, C. Monnet, J. Dussaud, S. Malato, J. Blanco, M.I. Maldonado, J.M. Herrmann, Appl. Catal. B Environ. 46 (2003) 319–332.
[41] C. Guillard, H. Lachheb, A. Houas, M. Ksibi, E. Elaloui, J.M. Herrmann, J. Photochem. Photobiol. A Chem. 158 (2003) 27–36.
[42] E. Puzenat, H. Lachheb, M. Karkmaz, A. Houas, C. Guillard, J.M. Herrmann, Int. J. Hydrogen Energy 5 (2003) 51–58.
[43] H. Cheng, J. Ma, Z. Zhao, L. Qi, Chem. Mater. 7 (1995) 663–671.

[44] A. Chemseddine, T. Moritz, Eur. J. Inorg. Chem. 1999 (1999) 235–245.
[45] H.P. Klug, L.E. Alexander, X-Ray Diffraction Methods for Polycrystalline and Amorphous Materials, John Wiley and Sons, NY, 1954.
[46] W.W. Yu, J.C. Falkner, B.S. Shih, V.L. Colvin, Chem. Mater. 16 (2004) 3318–3322.
[47] N. Serpone, E. Pelizzetti, Photocatalysis: Fundamentals and Applications, John Wiley & Sons, NY, 1989.
[48] A.K. Datye, G. Riegel, J.R. Bolton, M. Huang, M.R. Prairie, J. Solid State Chem. 115 (1995) 236–239.
[49] A. Selloni, A. Vittadini, M. Gratzel, Surf. Sci. 402–404 (1998) 219–222.
[50] A. Vittadini, A. Selloni, F.P. Rotzinger, M. Gratzel, Phys. Rev. Lett. 81 (1998) 2954–2957.